The Madden–Julian Oscillation in ECHAM6 and the Introduction of an Objective MJO Metric

TRAUTE CRUEGER, BJORN STEVENS, AND RENATE BROKOPF

Max Planck Institute for Meteorology, Hamburg, Germany

(Manuscript received 6 July 2012, in final form 23 October 2012)

ABSTRACT

This study presents a quantitative evaluation of the simulated Madden–Julian oscillation (MJO) in an ensemble of 42 experiments performed with ECHAM6 and previous ECHAM versions. The ECHAM6 experiments differ in their parameter settings, resolution, and whether the atmosphere is coupled to an ocean or not. The analysis concentrates on a few basic features of the MJO, namely, the signatures of convection/precipitation coupled with the circulation system and the eastward propagation strength of outgoing longwave radiation (OLR) and 850- and 200-hPa zonal winds within the MJO-related frequency–wavenumber range. It also examines whether precipitation and OLR show similar signatures in the MJO as simulated by ECHAM. The experiments reveal an MJO, however, to different degrees and in different aspects, so that a sound assessment requires a multivariate approach. In particular, the convective rainfall signatures are decoupled from the dynamic signature of the MJO in the simulations herein, which eventually leads to the introduction of a new MJO diagram and metric that incorporate OLR and the zonal winds in 850 and 200 hPa. The analysis here confirms the importance of the convection scheme: only with the Nordeng modifications to the Tiedtke scheme can realistic MJO features be simulated. High-resolution coupled experiments better represent the MJO as compared to low-resolution AMIP experiments. This is shown to follow from two more general findings, namely, that 1) air–sea interaction mainly increases the convective signature and 2) increased resolution enhances eastward propagation.

1. Introduction

The Madden–Julian oscillation (MJO) is the dominant mode of intraseasonal variability in boreal winter and/or spring in the equatorial tropics. Discovered by Madden and Julian (1971, 1972, 1994), its salient features are coherent eastward propagating patterns of enhanced and suppressed convection over the Indian Ocean, the Indo-Pacific warm pool, and the western Pacific Ocean. Because it describes an envelope of convective activity, and hence precipitation, the MJO is highly relevant for local and regional weather and climate. In addition, through its impact on the overall tropical circulation the MJO has nearly global impacts, for instance, on El Niño–Southern Oscillation (McPhaden 1999; Takayabu et al. 1999; Zhang and Gottschalck 2002; Teng and Wang 2003; Lau 2005; Pohl and Matthews 2007), the monsoon systems (Jones and Carvalho 2002; Goswami et al. 2003; Wheeler and McBride 2005; Straub et al. 2006), and the extratropics (Ferranti et al. 1990; Higgins and Mo 1997; Matthews et al. 2004; Cassou 2008; Vitart et al. 2011). Thus, a realistic representation of the MJO is important for climate modeling and numerical weather prediction. Although many general circulation models (GCMs) have improved representations of the MJO and theoretical work has greatly advanced our understanding of some of its necessary ingredients (Majda et al. 2007), many shortcomings remain (Park et al. 1990; Slingo et al. 1996, 2005; Lin et al. 2006; Sperber and Annamalai 2008).

It is generally accepted that the ability of a large-scale model to show an MJO depends on its representation of deep moist convection [Slingo et al. 1996; Maloney and Hartmann 2001; Lee et al. 2003; Lin et al. 2006; Zhu et al. 2009; Jia et al. 2008, 2010; see also Zhang (2005) for a review]. Crucial issues of the parameterization of convection are the convective triggering, the closure and the parameters for entrainment and detrainment, which define the cloud model. Many of the uncertain assumptions

Corresponding author address: Traute Crueger, Max Planck Institute for Meteorology, Bundesstrasse 53, D-20146 Hamburg, Germany.
E-mail: traute.crueger@zmaw.de

DOI: 10.1175/JCLI-D-12-00413.1

inherent in convective parameterization can be avoided through the use of superparameterization, wherein the deep convection scheme is replaced by a two-dimensional cloud-resolving model at each GCM grid point (Randall et al. 2003). The use of such an approach enhances eastward propagation of cloud clusters and greatly improves the representation of the MJO, thus supporting the idea that the convective representation is of paramount importance in representing the MJO (Khairoutdinov and Randall 2001; Benedict and Randall 2009, 2011). However, others (e.g., Liess et al. 2004; Sperber et al. 2005) have shown that it is also possible to simulate important features of the MJO with a GCM using parameterized convection. ECHAM has long stood out as one of the few general circulation models that has a reasonably good simulation of the MJO (Sperber 2004; Sperber et al. 2005; Lin et al. 2006; Sato et al. 2009; Kim et al. 2009; Sperber and Annamalai 2008); however, the reason why ECHAM was capable of simulating an MJO, whereas other models with parameterized convection failed, has not been systematically studied. Some authors (e.g., Sperber et al. 2005; Lin et al. 2006) have suggested that the link between the convective closure and the moisture convergence in ECHAM5, which is closely tied with the large-scale wave circulation that leads to a positive wave–heating feedback in the MJO, might be part of the reason.

Besides the representation of convection, other properties of the experimental configuration have also been shown to be important for a realistic simulation of the MJO. Liess and Bengtsson (2004) demonstrated that ECHAM4 produces realistic MJO-like variability and explored the effects of model resolution on the simulated MJO. They found that the MJO performance is linked to an appropriate ratio of vertical and horizontal resolution. On the other hand, Inness et al. (2001) found a better MJO when only the vertical resolution is doubled. Lin et al. (2006) argued that tropical precipitation, which accompanies MJO-like variability, may be improved by refining a model's moist physics. Jia et al. (2008), however, do not find fundamental differences among their experiments performed with three different resolutions of an atmospheric general circulation model (AGCM). The role of air–sea interaction has been examined by Sperber et al. (2005), who investigated the MJO in ECHAM4 with five different configurations, prescribed SSTs, and different ocean models. They only found a well-simulated MJO in those ECHAM versions that were coupled to an oceanic GCM (OGCM). In particular, ECHAM4/Ocean Isopycnal Model (OPYC) showed obviously an excellent representation of the MJO. Using ECHAM4, Liess et al. (2004) focused on the role of the underlying SSTs and atmosphere–ocean couplings in driving realistic MJO-like variability, but did not find improvements in response to coupling. Generally, the literature remains ambiguous on the role of air–sea coupling, where clear improvements (Waliser et al. 1999; Sperber et al. 2005; Woolnough et al. 2007), marginal improvements (Lin et al. 2006), minor impacts (Newman et al. 2009), and deterioration (Hendon 2000; Liess et al. 2004) of the MJO have all been found. The discussion of Zhang et al. (2006) on the role of air–sea interactions thus led to the suggestion to deal with this issue in more detail, for instance by focusing on the specific MJO properties that are affected by the coupling. Part of the contradicting results found in the literature come from the fact that different studies explore different models and different aspects and often use different metrics to assess the MJO, which makes it difficult to develop a clear picture.

This study is based on an ensemble of 37 ECHAM6 simulations, complemented by the analysis of five additional experiments using older versions of ECHAM. Thus, the results are not overly contaminated by large differences in model physics and metrics and facilitate a systematic analysis of factors thought to be relevant to the representation of the MJO: 1) the convection scheme, 2) horizontal and vertical resolution, and 3) fully interactive air–sea coupling. The analysis of these simulations is based on a consistent framework developed around the joint efforts of the community to collapse the assessment of MJO skill in climate simulations to a minimal set of diagnostics (Waliser et al. 2009; Kim et al. 2009; Subramanian et al. 2011). Additionally, the present analysis is extended to address the question whether outgoing longwave radiation (OLR) or precipitation is more appropriate to assess the MJO in climate simulations. This question arises in the simulation framework because the OLR depends on the properties of the cloud scheme while the precipitation depends on properties of the convective scheme, and there is no guarantee that these track each other. However, little systematic difference is seen between these two measures of the convective signal.

Our analysis additionally shows that many of the MJO metrics produced by the standard diagnostics scale well with one another, which motivates the development of a new diagram and metric of the MJO based only on those measures of the MJO that do not correlate well with one another in our simulations. This minimum set of measures involves the eastward propagation strength of the convective envelope and the strength of the OLR signal. This reduction helps clarify those factors that influence the representation of the MJO in ECHAM6, and the ways in which they do so. The robustness of our

findings is evaluated by additional simulations performed with previous ECHAM versions.

2. Methods

a. Model

The basis of our analysis is an ensemble of simulations performed with ECHAM6. The robustness of the obtained results is evaluated by additional experiments performed with ECHAM4 and ECHAM5. The ECHAM6 ensemble comprises 37 coupled and uncoupled Atmospheric Model Intercomparison Project (AMIP)-style experiments, performed with physically slightly different versions of the Earth System Model developed by the Max Planck Institute for Meteorology in Hamburg (MPI-ESM). The MPI-ESM consists of an atmospheric general circulation model ECHAM6 (Stevens et al. 2013) coupled to the MPI ocean model (MPI-OM) (Jungclaus et al. 2013). The main differences between ECHAM6 and ECHAM5 are that ECHAM6 is run at a default higher vertical resolution (i.e., 47 instead of 31 vertical levels), which leads to a better representation of the upper troposphere/ stratosphere; ECHAM6 incorporates completely new aerosol and surface albedo climatology and makes use of a new shortwave radiation scheme that is more accurate in offline tests and has less cloud absorption. The convection scheme used by all versions of ECHAM since ECHAM3 is the Tiedtke–Nordeng scheme. This scheme is based on Nordeng's (Nordeng 1994) modification to the original Tiedtke scheme, which was used by ECHAM3 (Tiedtke 1989, 1993), and also by the European Centre for Medium-Range Weather Forecasts (ECMWF), with minor modifications, for a number of years. Nordeng modified Tiedtke's representation of deep convection by relating organized entrainment and detrainment to convective activity itself. Deep convective organized entrainment takes place as an inflow of environmental air into the cumulus updraft when the cloud parcels accelerate upward (i.e., when the buoyancy is positive). Nordeng also modified Tiedtke's closure for deep convection so that it takes the form of a quasi-equilibrium closure wherein convective available potential energy (CAPE) is reduced to zero over a specified time scale. Differences between ECHAM4 and ECHAM5 exist with respect to the shortwave and longwave radiation and the treatment of land surface processes and data as discussed by Stevens et al. (2013) and Roeckner et al. (2003).

b. Data

The present analysis builds on the work of Waliser et al. (2009), who developed an MJO diagnostic package based on the investigation of precipitation, daily OLR as a proxy for convective precipitation, and daily zonal wind components, denoted by u at 850 and 200 hPa. Daily data are used with the climatological annual cycle removed.

1) OBSERVATIONS

For OLR we use the Advanced Very High Resolution Radiometer (AVHRR) measurements (Liebmann and Smith 1996). Winds are derived from reanalysis. Because the reanalysis of meteorological data is a rather indirect inference of the state of the atmosphere, we use several reanalysis products and take their spread as a rough indicator of the uncertainty. The products used in our analysis are the National Centers for Environmental Prediction (NCEP)–National Center for Atmospheric Research (NCAR) Reanalysis I (Kalnay et al. 1996), the 40-yr ECMWF Re-Analysis (ERA-40; Uppala et al. 2005), and the interim ECMWF Re-Analysis (ERA-Interim) data (Dee et al. 2011), each of them for the period of 1980 until 1999. Although it is appreciated that a reanalysis of meteorological observations will be influenced by the model underlying the reanalysis, it is also understood that observations are never model-free; hence we often refer to the combination of the reanalysis winds and the AVHRR measurements as ''observations.'' In so doing, it is understood that, in the case of the reanalysis winds, how one arrives at this observation may involve a greater leap of faith than is the case for some other types of observations.

2) EXPERIMENTS

A variety of uncoupled (AMIP style) and coupled simulations with different grid resolutions are evaluated. All experiments were performed during the development and tuning process of ECHAM 6 (Mauritsen et al. 2012). The experiments were not specifically designed for a study with respect to the MJO, but rather as an ensemble of opportunity that differed as a result of small parameter adjustments or changes in resolution on the way to a family of well-balanced coupled models. The set of experiments is listed in Table 1. The ECHAM6 experiments were accomplished with three different resolutions as the T63 model was run with both 47 vertical levels (hereafter low resolution, or LR), and with 95 vertical levels (hereafter mixed resolution, or MR). The T63 grid corresponds to a grid distance of about 1.9° (about 200 km at the equator). The increase of the vertical levels is associated only with a better resolution of the upper troposphere and stratosphere, beginning at about 500 hPa; 41 layers exist between 10 and 0.01 hPa. The midtropospheric resolution is about 40 hPa for both resolutions. Additionally, higher-resolution experiments were performed on a T127 grid with 95 vertical levels (hereafter high resolution, or HR). In the coupled

TABLE 1. Number of datasets of observations and experiments for a given model and model resolution (in parentheses: horizontal resolution) used in this study. The observational data include the AVHRR OLR combined with the winds of ERA-40, ERA-Interim, and NCEP, respectively.

			T127L95 (1°)	T63L95 (1.9°)	T63L47 (1.9°)	T63L31 (1.9°)	T42L19 (2.8°)	T31L19 (3.8°)
Observations		3						
ECHAM6	Coupled		9	6	10			
	AMIP		4	1	6			
	AMIP-Tiedtke				1			
ECHAM5	Coupled					1		1
	AMIP				1	1		
ECHAM4	AMIP						1	

experiments, the ocean grid for the LR experiments is a GR15L40 grid, which is based on a bipolar grid with a grid spacing of 1.5° at the equator. For the MR and HR experiments a tripolar ocean grid, TP04L40, which is both finer (at the equator the grid spacing is 0.4°) and more uniformly distributed relative to GR15L40, is employed. Both ocean grids have 40 vertical levels, with a topmost layer thickness of 12 m. The coupling time step between the atmosphere and the ocean model is once per day. Coupled and uncoupled experiments with different resolutions are incorporated into our ECHAM6 ensemble. Experiments at a given resolution may also differ with respect to minor parameter changes (Mauritsen et al. 2012) and minor bug fixes that occurred as part of the model development cycle. Because differences between any two experiments may involve several changes to the model, we are not able to attribute MJO changes to the distinct parameter changes. Instead, the experiments are used to document the range of MJO variability within broader groupings of coupled and uncoupled simulations with different resolutions.

All of the experiments in the ECHAM6 MJO ensemble, except for one (AMIP TIEDTKE), were performed with the Tiedtke–Nordeng convection scheme. The AMIP-TIEDTKE experiment uses the original Tiedtke scheme, without the Nordeng modifications (see section 2a), in an LR model configuration. The AMIP and atmosphere-only experiments were performed and analyzed from 1980 to 1999 and used observed anthropogenic forcing, such as greenhouse gases and aerosols and natural forcing, such as solar irradiance and volcanic activity, whereas the coupled simulations were performed under preindustrial conditions. Additionally, we examine a couple of experiments performed with ECHAM4 and ECHAM5. The latter was used in a coupled mode with the ocean model MPI-OM in a T63L31 and T31L19 resolution, and in AMIP mode in T63L31 and T63L47 resolution. One AMIP ECHAM4 experiment in T42L19 resolution is examined. The analysis of all experiments was performed over a 20-yr period, except for the simulation with ECHAM4, which was only run for 15 years.

c. Analysis

The processes involved in the MJO are complex and only partially understood, which makes a comprehensive investigation of the MJO difficult. For this reason, and out of a desire to maintain continuity with other work in the field, we focus our analysis around the Climate Variability and Predictability (CLIVAR) MJO simulation diagnostics developed and described by Waliser et al. (2009) and frequently applied by other investigators (e.g., Kim et al. 2009; Subramanian et al. 2011). We further focus on the most prominent features of the MJO, namely, the eastward propagation and the strength of the convective envelope (as measured by OLR or precipitation) and its accompanying circulation system. Formally, the analysis is centered on the nature of variability in the band of wavenumbers and frequency, and in regions where the MJO is most evident, hence MJO-like variability. Because we do not demonstrate that the processes that generate MJO-like variability are the same as those that underlie the real MJO, when we speak of the MJO in our model it should be taken for granted that we are referring to our model's representation of MJO-like variability.

A characteristic feature of the MJO is the signal of eastward propagating spectral power in fields related to precipitation and the zonal circulation at intraseasonal and planetary scales in the tropical belt (see, e.g., Zhang et al. 2006). A measure for this eastward propagation can be derived from frequency–wavenumber spectra. When the ratio R between the eastward (positive frequencies) and westward (negative frequencies) spectral power in a specific wavenumber/frequency range is greater than 1, we can speak of the eastward propagation as being dominant. For the MJO this range is for wavenumbers between 1 and 3 and for frequencies between 1/100 day^{-1} and 1/20 day^{-1} (representing the periods between 20 and 100 days). To calculate R, we

use data around the entire equatorial belt [which, following Waliser et al. (2009), is meridionally averaged from 10°S to 10°N] and calculate the ratios for each of the analyzed fields separately. Our focus on R as a measure of the strength of the MJO follows the work of a number of other authors (e.g., Zhang et al. 2006; Kim et al. 2009; Sobel et al. 2010; Kim et al. 2011). Throughout this article we refer to R_{OLR} for OLR, R_{u850} for u at 850 hPa, and R_{u200} for u at 200 hPa. We further define a mean propagation ratio R_{mean} as the arithmetic mean of eastward to westward spectral power ratio in the respective wind components and the corresponding ratio for OLR.

A tool to describe the coupling between circulation, as measured by the zonal wind signature, and precipitation is the multivariate empirical orthogonal function (EOF). Following Waliser et al. (2009), we derived the multivariate EOFs from u_{850} and u_{200} and OLR around the equatorial belt. The leading pair of these EOFs can help to assess the MJO in a simulation (Wheeler and Hendon 2004). The leading EOFs derived from simulations often explain considerably smaller amounts of fractional variance than the leading EOFs derived from observations, especially for OLR (Waliser et al. 2003, 2009; Zhang et al. 2006; Kim et al. 2009). For this reason, Waliser et al. (2009) argued that F, the fractional variance that is explained by the multivariate EOF, is itself a quantitative measure of a model's skill in simulating the MJO.

We follow Waliser et al. (2009) and calculate the multivariate EOFs of the 20–100-day bandpass filtered (Duchon, 1979) anomalies of OLR and zonal winds at 850 and 200 hPa, first averaged over 15°S to 15°N. The data are standardized (through normalization by their variance) before combining them in one field and calculating the EOFs (von Storch and Zwiers 1999). We evaluate the sum of the explained fractional variances of the two leading EOFs produced for each of the three individual fields (one for OLR and the other two for the winds) and their mean. Here, F_{OLR}, F_{u850}, and F_{u200} denote the fraction of the explained variance for OLR, u_{850}, and u_{200}, respectively, and their arithmetic mean is denoted by F_{mean}.

3. Results

First, we present a qualitative diagnostic of 20-yr periods for three experiments, and, as a reference, the ERA-40 zonal winds and the AVHRR OLR from 1980 to 1999. The three experiments consist of one T63L47 (LR) AMIP experiment, one T127L95/TP04 (HR) coupled experiment, and the AMIP-TIEDTKE (T63L47) experiment. Hereafter we analyze all 42 experiments by considering the quantities described in section 2c.

a. Qualitative assessment of the MJO

The main characteristic of the MJO is the eastward propagating systems of enhanced and suppressed convection and their corresponding zonal wind fields. At a glance these features are apparent from Fig. 1, which shows the life cycle of the MJO separated into eight phases as constructed by compositing the u_{850} winds and OLR over the sum of the square of the first two principal components (i.e., $\mathrm{PC1}^2$ and $\mathrm{PC2}^2$) of the multivariate EOFs, which are shown in Fig. 2 and discussed below. The compositing threshold is defined to be larger than one. The phases of the MJO life cycle are obtained from the phase relationship between PC1 and PC2 following Waliser et al. (2009) and Wheeler and Hendon (2004); see also section 2c. For the observations, negative AVHRR OLR anomalies, representing enhanced convection, appear during the first two phases (corresponding to the panels in rows 1 and 2 of Fig. 1, top left) in the Indian Ocean, during which easterly winds prevail east of the deep convection. Suppressed convection still dominates over the warm pool area. During the mature phases (rows 4–6), the center of deep convection propagates eastward and intensifies, while suppressed convection becomes increasingly pronounced over the Indian Ocean. During this phase enhanced convection is accompanied by westerly winds in the lower troposphere. Farther to the east, convection weakens and disappears around the date line. Clearly recognizable is the phase relationship between the spatial structures of OLR and the wind. The HR coupled experiment captures the observed features reasonably well: the circulation pattern shows strong similarities with the reanalysis, namely, the relationship between low-level westerly (easterly) winds and enhanced (suppressed) convection. Convection also disappears near the date line, which is also seen in the observations (Fig. 1, top right).

It is readily apparent that the representation of the MJO in the LR AMIP experiment compares less favorably to the observations (Fig. 1, bottom left). In the AMIP simulation the convective signal is weaker, in all respects, than in the observed and also weaker than in the HR coupled experiment. Although the LR AMIP experiment is not a particularly compelling simulation, an MJO signal is at least discernible. This is in contrast to the AMIP-TIEDTKE experiment, which shows no evidence of an eastward propagating convective envelope. Patterns of enhanced and suppressed convection are hardly obvious and no relationship between the winds and the OLR is obtained (Fig. 1, bottom right). Thus, within our ECHAM6 ensemble, the AMIP-TIEDTKE

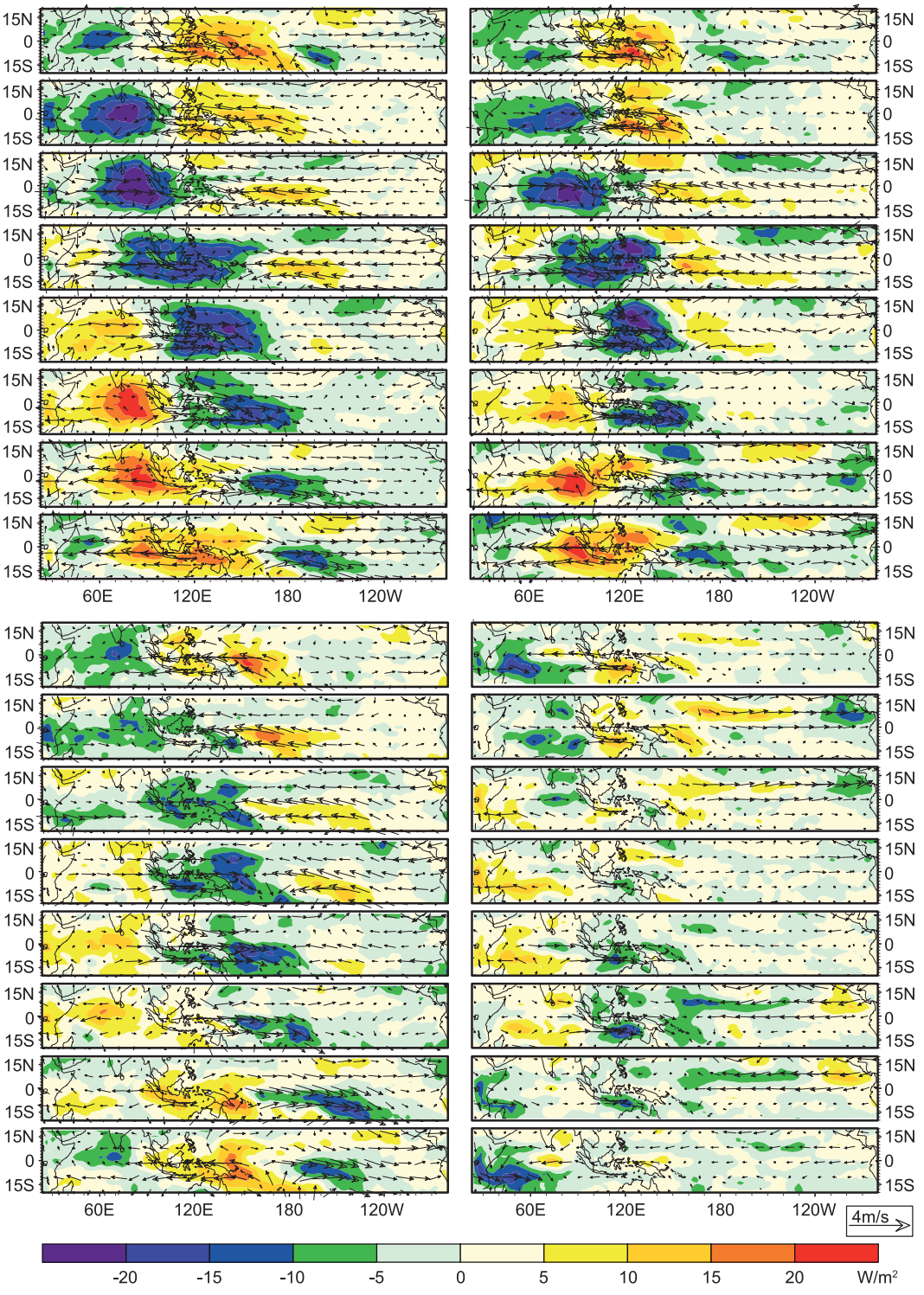

FIG. 1. Composite November–April 20–100-day filtered OLR (blue/green: enhanced convection; yellow/orange: suppressed convection) and 850-hPa wind anomalies (vectors) as a function of the MJO phase. The composite is based on $PC1^2 + PC2^2 > 1$ (see text for more information). (top left) ERA-40/AVHRR (1980–99); (top right) coupled T127L95; (bottom left) AMIP T63L47; (bottom right) AMIP-TIEDTKE (T63L47).

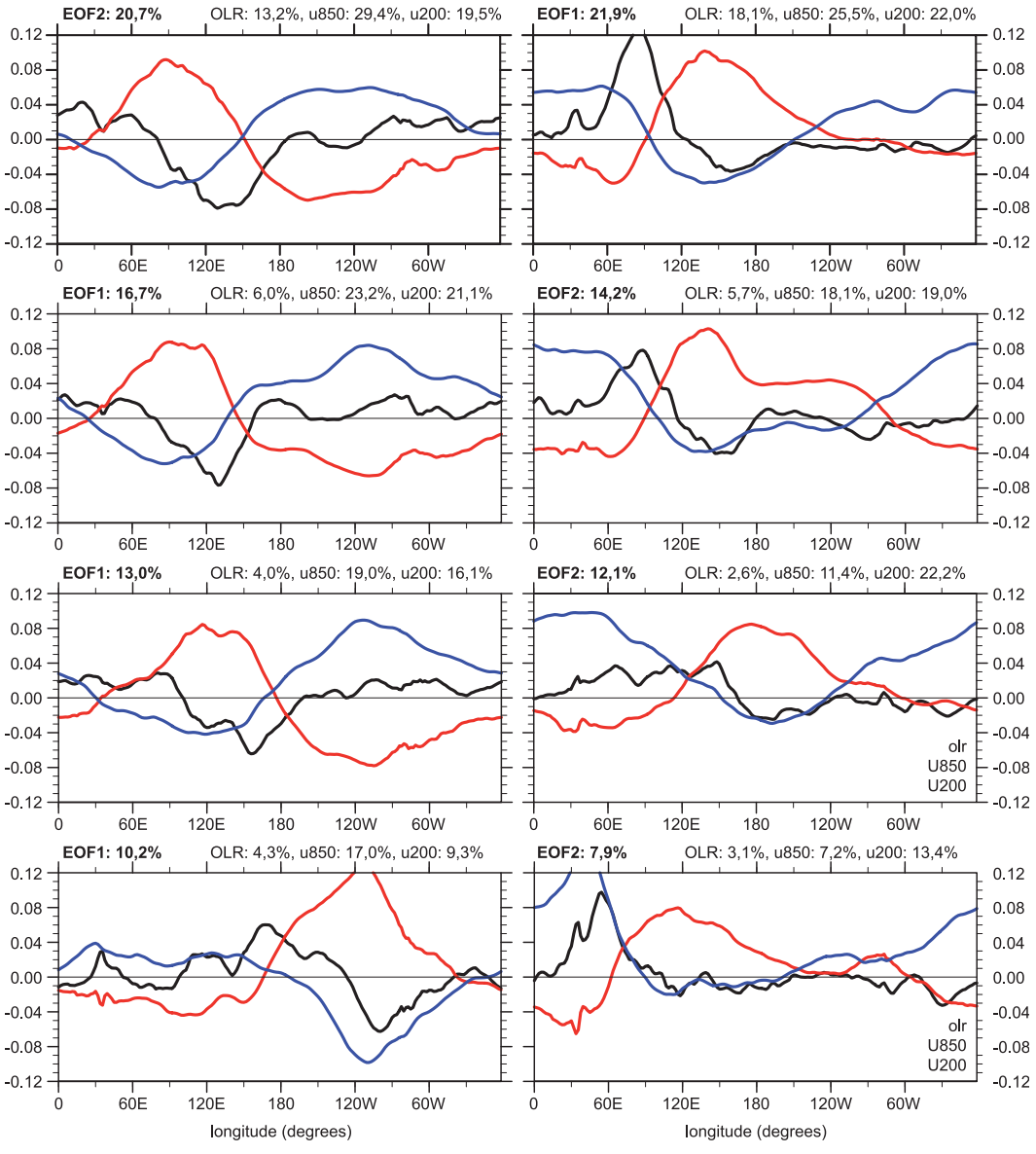

FIG. 2. First two multivariate EOFs of 20–100-day filtered 15°S–15°N averaged zonal winds at 850 (red) and 200 hPa (blue) and OLR (black). (top) ERA-40 winds and AVHRR OLR (1980–99), (second row) coupled T127L95; (third row) AMIP T63L47; (bottom) AMIP-TIEDTKE. The total explained variance by each mode is shown at the top left, and the explained fractional variances of the individual fields at the top right of each figure. (Note that for comparison reasons EOF1 and EOF2 for ERA-40 are exchanged).

experiment serves as an example of a poor MJO representation, one that is not untypical of a large class of atmospheric general circulation models that do not produce a recognizable signature of the MJO. The main difference between Nordeng's modified Tiedtke scheme and the original Tiedtke scheme used in AMIP-TIEDTKE is that the former is much more sensitive to tropospheric moisture (Möbis and Stevens 2012).

The life cycles displayed in Fig. 1 are based on the leading pair of the multivariate EOFs. For the same four datasets these EOFs are shown in Fig. 2. The EOFs derived from the observations (including reanalysis data for the winds) reveal the characteristic features of the MJO, namely, 1) an out-of-phase relationship between the u_{850} and u_{200} anomalies; 2) positive (westerly) u_{850} anomalies west of enhanced convection over the Indian Ocean early in the life cycle of the MJO; 3) u anomalies more in phase with enhanced convection in the west Pacific; 4) strong OLR anomalies only in the eastern hemisphere, whereas circulation anomalies are strong

around the entire equator; 5) strong convective suppression over the Indian Ocean, when enhanced convection is found in the west Pacific area; and 6) roughly the same amount of intraseasonal variance in the two leading EOFs. (The last point explains why, in Fig. 2, EOF1 and EOF2 of ERA-40 are exchanged, as the labeling depends arbitrarily on whichever one happens to explain the most variance.) These features are well captured by the HR coupled simulation; however, the convective signals are somewhat weaker and the circulation pattern in EOF2 differs from the corresponding EOF derived from the observations (here EOF1) east of the date line. In both EOF1 and EOF2, the phase relationship between OLR and the u_{850} is similar to that in the observations. These features are also evident in the LR AMIP experiment, although differences in the EOF basis between it and the observations are even more pronounced than in the coupled run, especially in EOF2. Although in EOF1 enhanced convection is only shifted toward the east, the strong structure of enhanced and suppressed convection obtained in EOF2 of the HR coupled experiment is substantially underestimated in the AMIP LR run. The EOFs for AMIP-TIEDTKE stand in marked contrast to those of the other two simulations. EOF1 reveals the strongest signals east of the date line, contrary to what is observed. EOF2 shows convection anomalies over the western Indian Ocean, but negligible anomalies over the warm pool area and the west Pacific. Thus, AMIP-TIEDTKE represents an example of a simulation that does not produce a correct phase relationship between equatorial convection and wind anomalies. This deficiency is often found in state-of-the-art AGCMs (e.g., Maloney and Hartmann 2001).

Generally, for all variables, the fractional variances of intraseasonal variability explained by the sum of the two EOFs are smaller in the simulations than in the observations. This is especially apparent for OLR, which is a factor of 2 larger in the observations than it is in even our best experiments. These results agree with earlier work by Kim et al. (2009), who also found for a couple of GCMs [e.g., the NCAR and Geophysical Fluid Dynamics Laboratory (GFDL) models] that the convective signal is not as well represented as the dynamic signal. Thus, the weaknesses obvious in the life cycle patterns are also mirrored by the EOFs (on which the life cycles are based) and expressed by an inability of the leading pairs of EOFs to explain a sufficient amount of the fractional and total variances of the intraseasonal variability. This supports the suggestion of Waliser et al. (2009) to use these explained fractional and total variances of intraseasonal variability as a quantitative measure of the skill with which a GCM is able to simulate the MJO and hence motivates the incorporation of these measures in our assessment of the MJO.

As mentioned above, one crucial MJO feature is the eastward propagation of the convective envelope for periods from 30 to 80 days and for wavenumbers 1–3. Thus, according to what we described in section 2c, we expect a concentration of spectral power within this range for positive frequencies and hence $R > 1$. For the observations (i.e., the AVHRR-derived OLR and the reanalysis winds), we see a clear predominance of power within the MJO frequency–wavenumber envelope, so that values of R are around 4 (4.6, 4.1, and 3.5 for R_{OLR}, R_{u850}, and R_{u200}, respectively; e.g., Figs. 3a–c). In the spectrum for u_{200}, the MJO is represented by the relative maximum at wavenumber 1 from 30- to 80-day periods (Fig. 3c). Relative to the observational data, both the coupled HR and the AMIP LR simulations yield partly too much power. However, in this respect, and qualitatively, the shapes of the HR coupled experiment spectra show a better correspondence to the observations than those from the LR AMIP run, although the coupled T127L95 version shows unrealistic high power at wavelengths larger than 3 for the OLR spectrum. The spectrum for u_{200} also shows a relative maximum at wavenumber 1 for the MJO frequencies. However, a clear overestimation of power for long periods is also evident. Spectral maxima of the coupled HR run for the three variables are found for the same wavenumbers and frequency ranges as in the observations (Figs. 3d–f). This is not the case for the LR AMIP experiment, whose peaks are outside the ranges of the observed MJO (Figs. 3g–i). As a consequence, the ratios of the eastward and westward spectral power within the MJO ranges are only half as large as those of the observations. However, R is still larger than one and thus represents eastward propagation (Figs. 3g–i). Values of R for the HR coupled simulation show more similarity to values derived from the observations, which are only slightly larger. The AMIP-TIEDTKE experiment shows hardly any correspondence with the spectra of the observations: The power is generally too weak, and in addition, it exhibits similar power for positive and negative frequencies and no maxima in the 30–80-day range: R is less than one, and thus the simulation does not represent eastward propagation (Figs. 3j–l).

Figures 1–3 demonstrate that ECHAM6 is able to reproduce an MJO, especially for coupled simulations at high resolution. The low-resolution AMIP version also produces a recognizable MJO and, while still better than many models, it performs consistently less well than does the high-resolution coupled model. To what degree these differences among our model versions are caused by differences in model resolutions or to air–sea coupling is analyzed in the following.

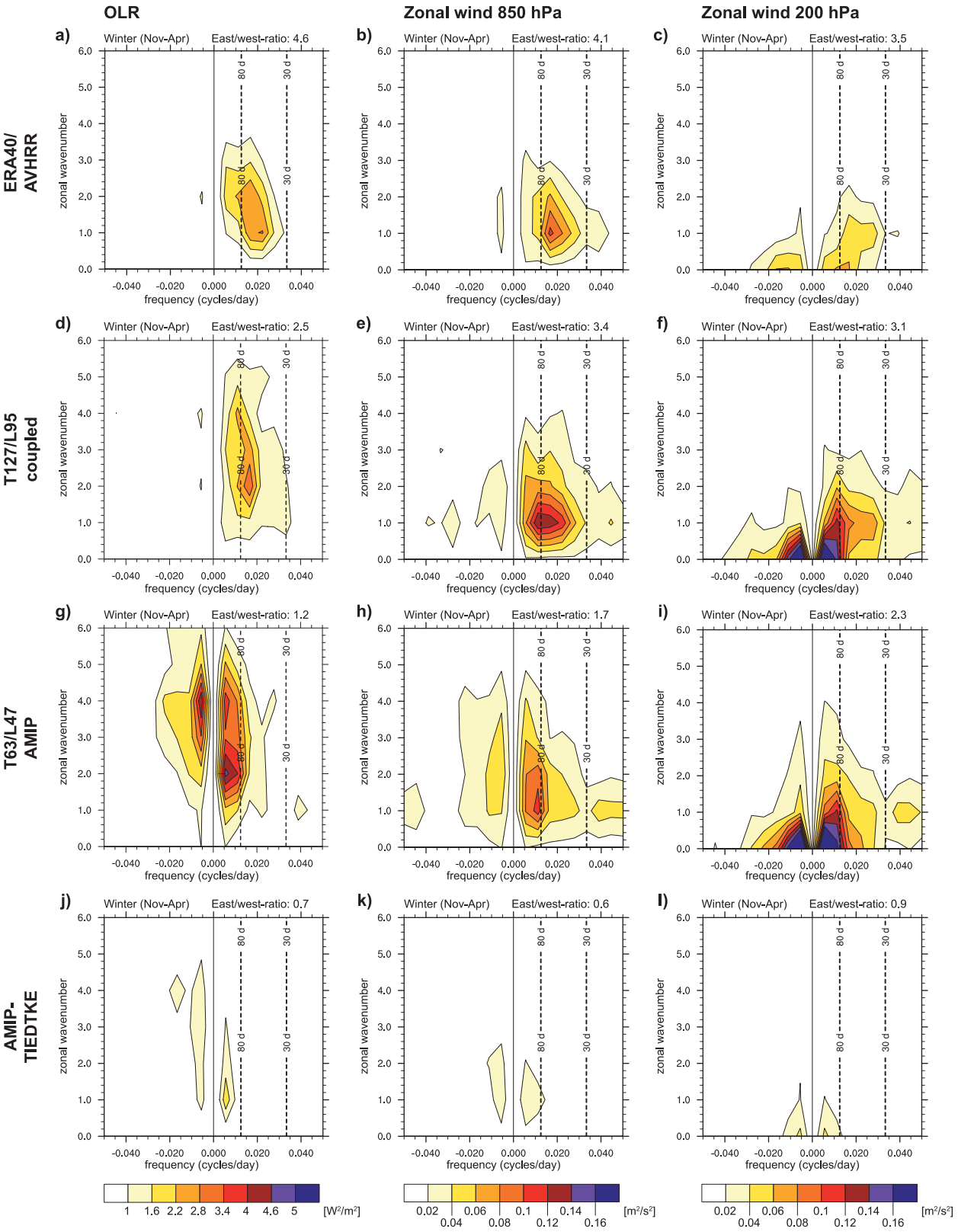

FIG. 3. Frequency–wavenumber spectra of 10°S–10°N and November–April averaged (left) OLR, and (middle) 850- and (right) 200-hPa zonal wind. (a) AVHRR OLR, (b),(c) ERA-40 (1980–99), (d)–(f) coupled T127L95, (g)–(i) AMIP T63L47, and (j)–(l) AMIP-TIEDTKE.

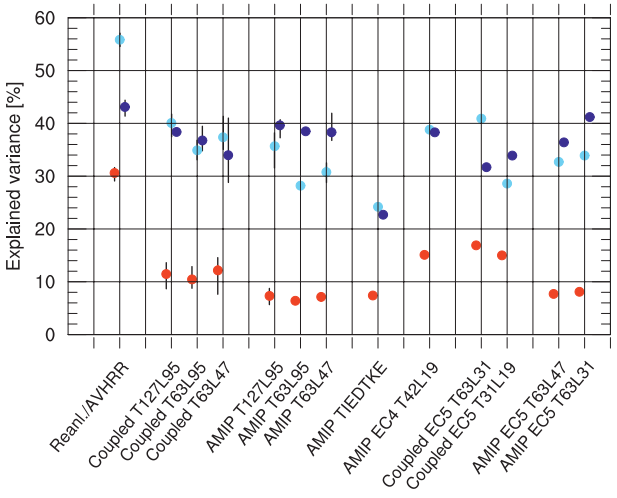

FIG. 4. Fractional explained variances F of multivariate EOFs of 20–100-day filtered and 15°S–15°N averaged OLR and 850- and 200-hPa zonal winds. Dots show the mean for each experiment group. Red indicates OLR; light blue, 850-hPa zonal wind; and blue, 200-hPa zonal wind. Vertical black lines represent the range among the simulations within an experiment group.

b. *Quantitative assessment of the MJO*

In the following, we analyze the observational and model datasets summarized in Table 1. We maintain our focus on the fraction of the explained variances of intraseasonal variability F and the eastward/westward propagation ratios R as introduced in section 2c. Generally, we evaluate the mean values of the distinct experiment groups (Table 1). In this section, we also examine whether the use of OLR, as compared to precipitation directly, impacts our results. To do so, we additionally calculate the precipitation spectra and perform the multivariate EOF analysis directly with precipitation instead of OLR.

Overall, observations have larger values of F than do the experiments, especially for OLR. This is apparent from Fig. 4 and Table 2. In both the experiments and in the observations, the amount of variance explained by the leading EOFs is larger for the winds than it is for the OLR. For the reanalysis winds, roughly half of the intraseasonal variance can be explained by the first two EOFs; this is much larger than for OLR, as F_{OLR} is only about 30%. Also the observed R values are generally larger than for the experiments, especially for OLR (Fig. 5). For u_{200} and u_{850}, the differences among the reanalyses are small. As was evident in the analysis of the ratio of eastward to westward spectral power in the MJO frequency–wavenumber envelope, the AMIP-TIEDTKE run does not yield a realistic representation of the explained variances in the MJO envelope. The fractional explained variances of the zonal winds of the AMIP-TIEDTKE simulation reveal lower percentages than those of the LR AMIP simulations, and point to substantial differences of the MJO as compared to the standard ECHAM6 AMIP simulations (Fig. 4), which incorporate Nordeng's modifications to the Tiedtke scheme.

1) IMPACT OF RESOLUTION

Eastward propagation, as measured by R in our analysis, is favored in coupled and high-resolution simulations, although the effects of resolution appear to

TABLE 2. Ratios of the eastward/westward propagation power R within the MJO frequency–wavenumber ranges (20–100-day period, wavenumbers 1–3) for the single equatorial fields of OLR, precipitation, and the zonal wind components at 850 and 200 hPa (R_{OLR}, R_{pre}, R_{u850}, and R_{u200}) and the mean of R_{OLR}, R_{u850}, and R_{u200} called R_{mean}. Also shown are fractional and total explained variances (F_{OLR}, F_{pre}, F_{u850}, F_{u200}, and F_{mean}) of the two first leading modes of the multivariate EOF derived from 20- to 100-day filtered 15°S–15°N averaged zonal winds at 850 and 200 hPa and OLR or precipitation, respectively. The numbers for AMIP-T63L95 are in parentheses, because these represent only one experiment.

		Ratios of eastward/westward propagation R					Fractional explained variance of multivariate EOF F				
	Experiment group	R_{OLR}	R_{pre}	R_{u850}	R_{u200}	R_{mean}	F_{OLR}	F_{pre}	F_{u850}	F_{u200}	F_{mean}
Observations		4.6		4.1	3.5	4.1	30.6		55.8	43.1	43.2
ECHAM6	AMIP T63L47 TIEDTKE	0.7	0.6	0.6	0.8	0.7	7.4	4.7	24.2	22.7	18.1
	AMIP T63L47	1.4	1.3	1.7	2.3	1.8	7.1	6.4	30.7	38.6	25.5
	AMIP T63L95	(1.3)	(1.2)	(1.8)	(2.1)	(1.7)	(6.4)	(5.5)	(28.2)	(38.5)	(24.3)
	AMIP T127L95	2.1	2.0	2.5	2.1	2.2	7.4	8.9	35.7	39.6	27.6
	Coupled T63L47	1.9	1.6	1.8	1.8	1.8	12.1	10.0	37.0	35.0	28.3
	Coupled T63L95	1.8	1.6	1.9	2.2	2.0	10.5	8.3	34.9	36.8	27.7
	Coupled T127L95	2.7	2.4	3.3	2.8	2.9	11.4	9.6	40.1	38.2	30.0
ECHAM5	Coupled T63L31	2.1	2.1	2.3	2.3	2.2	16.9	17.9	40.9	31.7	24.8
	Coupled T31L19	1.0	0.9	1.2	1.4	1.2	15.0	16.3	28.6	33.9	25.8
	AMIP T63L47	1.4	1.6	2.1	1.9	1.8	7.7	9.1	32.7	36.4	25.6
	AMIP T63L31	1.6	1.9	2.5	2.2	2.1	8.1	8.6	33.9	41.2	27.7
ECHAM4	AMIP T42L19	2.1	1.7	2.8	2.8	2.6	15.1	6.3	38.8	38.3	30.7

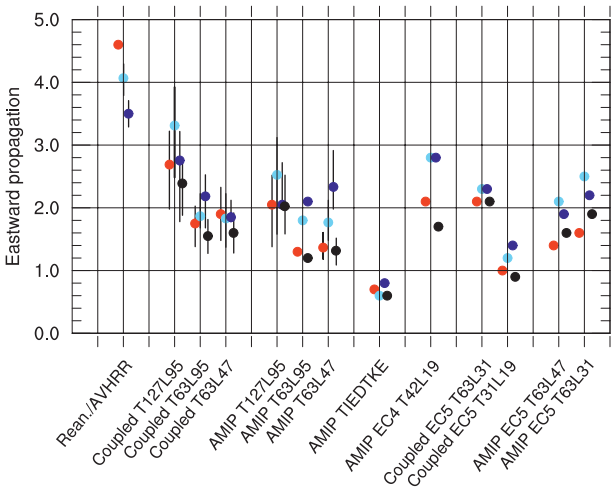

FIG. 5. Ratios of eastward/westward propagation power R within the MJO frequency–wavenumber ranges (see text). Black indicates precipitation; red, OLR; light blue, 850-hPa zonal wind; and blue, 200-hPa zonal wind. Vertical black lines represent the range among the simulations within an experiment group.

dominate. This is evident in Fig. 5 and Table 2. Note that R_{mean} increases from 1.8 (mean of all LR coupled and AMIP experiments) to 2.6 (mean of all HR coupled and AMIP experiments) in going from low to high resolution (LR vs HR), when averaged over all ECHAM6 simulations with a given resolution (irrespective of coupling). The coupled experiments are most responsive to resolution increases: R_{mean} increases from 1.8 for the LR configuration to 2.9 for the HR configuration. In the uncoupled (AMIP) experiments the increase is much more modest, with values of 1.8 and 2.2 for the LR and HR versions, respectively. Thus, increasing resolution from LR to HR enhances eastward propagation, predominantly in the coupled runs. Horizontal resolution appears to be more important than vertical resolution in producing larger values of R as, if anything, there is a slight reduction in R if only vertical resolution is increased (i.e., comparing LR and MR simulations). We note that those conclusions are not sensitive to whether R_{pre} or R_{OLR} is used (i.e., how the precipitation signal is measured). Overall the results obtained for ECHAM6 suggest that as simulations become more realistic in their representation of the propagation of the MJO, both through the incorporation of more scales of motion and coupling, the signal of eastward propagation in the MJO envelope improves.

A dependency of F on resolution is only obvious for the zonal winds, which are a few percentage points higher in the LR than in the HR versions; F_{OLR} also barely responds to resolution changes (Fig. 4; Table 2). The results obtained from the ECHAM6 ensemble are generally consistent with ECHAM5 simulations: an increase of vertical and horizontal resolution enhances eastward propagation, and changing only vertical resolution has a minor effect.

2) IMPACT OF AIR–SEA INTERACTION

The experiments show systematic differences between the AMIP and coupled runs. The value of F_{OLR} of the AMIP is less than one-fourth of what is observed. In the coupled simulations, F_{OLR} increases to about one-third of what is observed. Also, F_{u850} is smaller in the AMIP simulations than it is in the coupled runs (37% for the coupled runs, 32% for AMIP, 56% for reanalysis), but these differences are not as substantial as those for F_{OLR}. The value of F_{u200} is most similar to what is observed, and this quantity also appears less sensitive to the coupling. As mentioned previously, the east/west ratios are on average larger in the coupled than in the uncoupled ECHAM6 experiments, and more so at high resolution. In ECHAM5, the impact of air–sea interaction is even stronger: the convective signatures in the multivariate EOF strongly increase in response to coupling (comparing T63L31 coupled and AMIP experiments) (Fig. 4). Actually the highest F_{OLR} values are obtained for the coupled ECHAM5 experiments. Additionally, air–sea interaction slightly enhances the east/west ratios of OLR and precipitation in ECHAM5.

3) MJO–OLR AND MJO–PRECIPITATION RELATIONSHIP

Because the relationship between OLR and precipitation in nature is not necessarily the same as it is in the simulations, it was investigated to what extent our findings depended on how precipitation was measured in the simulations. To do so, we repeated much of the analysis discussed above using the simulated precipitation directly, rather than the OLR. Doing so makes it difficult to compare with observations, for which precipitation is generally not directly observed, but it gives an indication as to how robustly the simulated OLR measures MJO-like variability in the simulated precipitation.

Overall, we found little evidence of a systematic dependence of our analysis, and hence findings, as to whether or not precipitation is used directly or substituted by OLR. Only for the somewhat shorter experiments (15 yr) using ECHAM4 did we find an appreciable sensitivity to how precipitation was measured in the model. Although there was a tendency for F_{OLR} to be slightly larger than the fractional explained variance of precipitation F_{pre} in all the simulations, this difference was very pronounced in ECHAM4 (Fig. 6). The shorter simulation that is available for ECHAM4 (it is no longer possible to run this model) raises the possibility that this is an artifact, but we also note that ECHAM4 has a higher fraction of large-scale precipitation in the tropics than does either

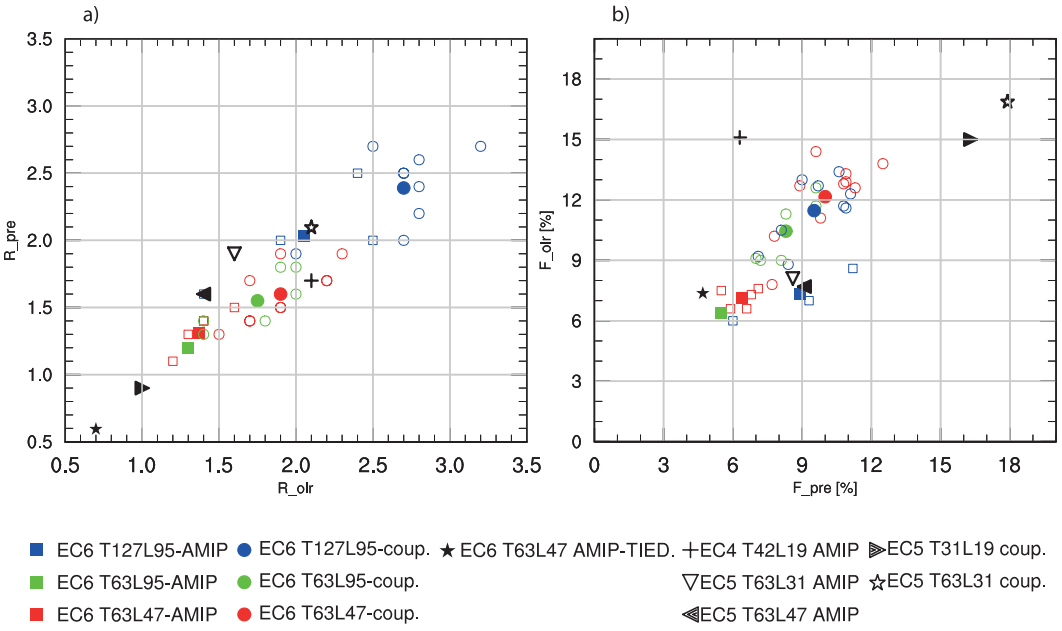

FIG. 6. Scatter of (a) east/west ratios of the spectra of precipitation R_{pre} and OLR R_{OLR}, and (b) fractional explained variances of OLR F_{OLR} and precipitation F_{pre} of multivariate EOF derived from the zonal winds in 850 and 200 hPa, and OLR and precipitation, respectively. Filled symbols indicate the mean of experiment group; open indicate single simulations.

ECHAM5 or ECHAM6, hence the differences may be real.

Our analysis suggests that there is a basis for being cautious when interpreting the model's OLR signal as representative of precipitation but that, for the ECHAM5 and ECHAM6 experiments on which the bulk of our analysis is based, this is probably feasible.

c. *Metric for the MJO*

The joint efforts of the community (e.g., Waliser et al. 2003, 2009; Zhang et al. 2006; Kim et al. 2009, 2011) to collapse a diverse set of diagnostics into a relatively small number of quantities that can be used to measure the skill with which a model represents the MJO made much of the present analysis possible. The question arises as to whether these metrics can be further reduced, at least for the purpose of evaluating our simulations. In effect this raises the question of relationships between the various quantities identified in the MJO diagnostics we have explored. To the extent that a single quantity provides a first indication of the MJO representation by ECHAM6, which as far as climate models is concerned has a good representation of the MJO, it might also prove useful for the analysis of other models.

For the ensemble of experiments performed by ECHAM, one quantity can often be a good proxy for another. Especially the R values of the different variables are correlated (e.g., R_{u850} and R_{u200}; Fig. 7a). On the other hand, the explained variances in different quantities are less well correlated; in particular, F_{OLR} (or F_{pre}) shows little relation to the other F quantities (e.g., F_{u200}; Fig. 7b). Therefore, in evaluating the present simulations, at least two quantities need to be considered: 1) the eastward propagation and 2) the strength of the precipitation signal. Because the R of OLR (or precipitation) and the zonal winds are reasonably well correlated, one of these quantities (or their mean) could be sufficient to describe the eastward propagation. We propose to utilize the mean of the three numbers R_{mean} because it is likely a more robust representation of the eastward propagation strength of the convective envelope.

Because the strength of the convective signature F_{OLR} is barely correlated with the other quantities it merits separate consideration. Moreover, F_{OLR} is a crucial quantity because it is considerably underestimated, even in our best simulations. Therefore, the second MJO characteristic that we explicitly account for in our MJO score is F_{OLR}. This motivates the introduction of the metric MJO_{sc} as a useful measure of the MJO:

$$\text{MJO}_{\text{sc}} = \sqrt{[\max(1, R_{\text{mean}}) - 1] \cdot F_{\text{OLR}}/100}. \quad (1)$$

In Eq. (1), $\max(1, R_{\text{mean}}) - 1$ assures that MJO_{sc} is set to zero if R_{mean} is less than one; that is, in the absence of eastward propagation dominating we do not find it

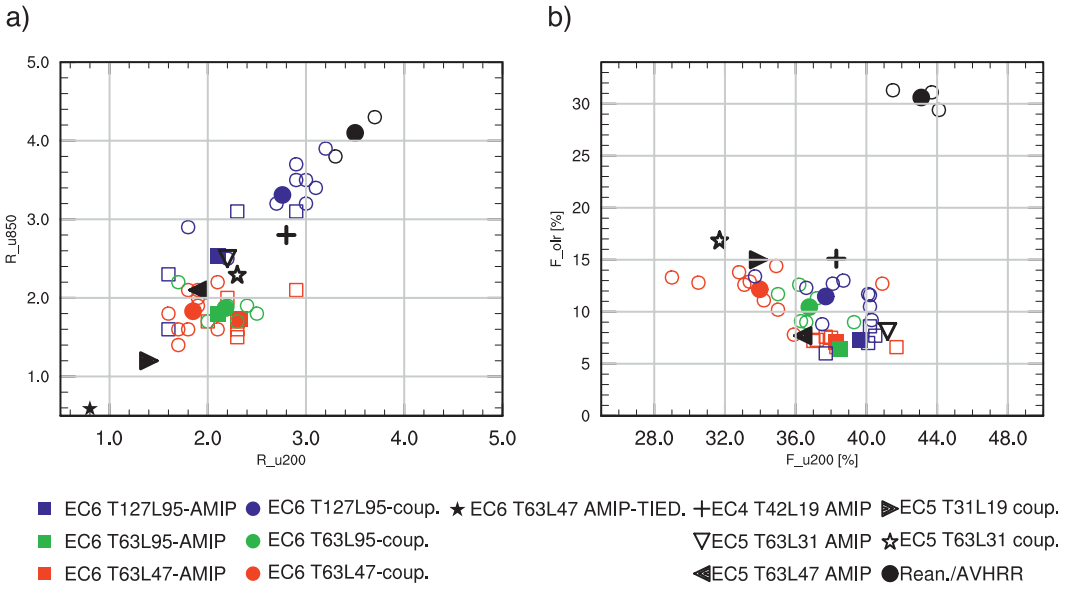

FIG. 7. Scatter of (a) R_{u850} and R_{u200} and (b) F_{OLR} and F_{u200}. Filled symbols indicate mean of experiment group; open symbols are for single simulations.

meaningful to speak of an MJO (see section 3a). The two quantities R_{mean} and F_{OLR}, which are utilized to derive $\mathrm{MJO_{sc}}$, are shown in a scatterplot in Fig. 8. Note that R_{mean} and F_{OLR} are neither correlated in the entire set of experiments nor in the distinct groups. The semicircles in Fig. 8 demarcate combinations of R_{mean} and F_{OLR} that yield the same $\mathrm{MJO_{sc}}$. The highest values of $\mathrm{MJO_{sc}}$ are found for the different reanalysis winds combined with the AVHRR OLR (Fig. 9). These observation-based values of $\mathrm{MJO_{sc}}$ show little spread, thus indicating

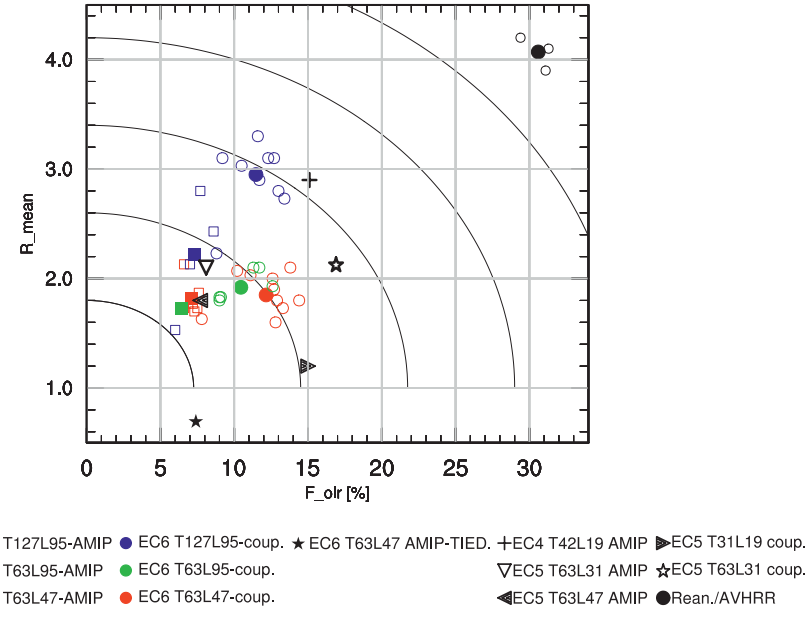

FIG. 8. Scatter of mean ratios of eastward/westward propagation power within the MJO frequency–wavenumber ranges for OLR and the zonal winds at 850 and 200 hPa (mean of R_{OLR}, R_{u850}, and R_{u200}) and fractional explained variance of the first two leading modes of precipitation component F_{OLR} for the experiments (see text for more information). Filled symbols: mean of experiment group; open symbols: single simulations.

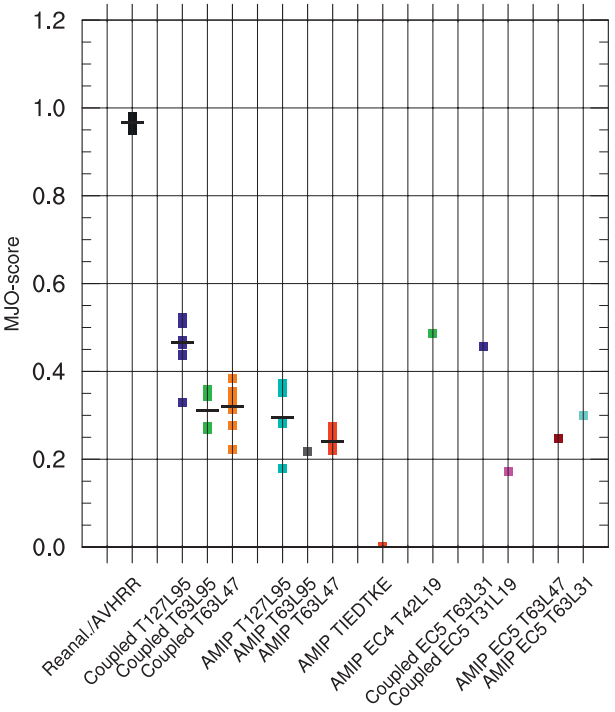

FIG. 9. MJO performance derived from Eq. (1). The black bar denotes the mean for the corresponding group.

the robustness of our metrics. The MJO_{sc} of the experiments is generally smaller than for the reanalysis. The AMIP-TIEDTKE experiment has a zero MJO_{sc}. This coincides with the results of section 3 that do not show eastward propagation for the AMIP-TIEDTKE simulation. In contrast to this simulation, the other simulations, all performed with the Tiedtke–Nordeng scheme, have positive MJO_{sc}. Thus, MJO_{sc} stresses the dependency of the simulated MJO on the formulation of the convection. As to be expected, the highest MJO_{sc} values of the ECHAM6 experiments are found for the coupled HR simulations. Generally, larger MJO_{sc} values are obtained for coupled as compared to uncoupled (AMIP) simulations. This is found for all resolutions and confirms the results found in the previous sections. In addition, higher resolution (T127L95 compared to T63L47) robustly enhances the MJO_{sc}, as scores for the T127L95 model are on average larger than those for the T63L47 model. The numbers for AMIP increase by 20% in response to resolution. For the coupled experiments a 50% increase is found. The T63L95 experiments do not show an improvement with respect to the T63L47 experiments.

Generally, the ECHAM5 scores confirm the results obtained from the ECHAM6 simulations: Coupling and the increase of horizontal and vertical resolution strengthen the MJO, while the increase of middle and upper troposphere resolution does not improve the MJO. Additionally, a very high MJO performance is found for the coupled T63L31 ECHAM5 simulation, which is as high as the average of the ECHAM6 coupled HR experiments. For the ECHAM4 simulation, the MJO performance is also high. This is also the only experiment that reveals considerably different MJO_{sc} depending on whether we use OLR or precipitation to measure convection in our metric. This is expected from the results above, which revealed a decoupling between OLR and precipitation in this previous ECHAM version.

Note that MJO_{sc} incorporates measures of the main MJO features. In particular, it requires predominantly eastward propagation at intraseasonal time scales as a necessary condition of the MJO. We are aware that the interpretation of this metrics needs some caution: because it does not include departures from observed quantities, the metric could achieve a realistic magnitude when one included quantity (F_{OLR} or R_{mean}) is overestimated while the other is underestimated. In addition, opposite-signed changes of the two considered quantities could not be separated by the metric, which is a general issue for simplified metrics or indices. Therefore, we strongly recommend the additional use of the MJO diagram (Fig. 8), which allows for such a separation. Nevertheless, we believe that MJO_{sc} is a simple metric that usefully summarizes important features of the representation of the MJO in ECHAM6.

4. Conclusions and outlook

This article investigates the representation of the MJO in an ensemble of 37 ECHAM6 simulations and additional experiments performed with ECHAM4 and ECHAM5. The ECHAM6 ensemble samples the effects of both structural and parameter sensitivity. Simulations were performed with different resolution, both in the vertical and the horizontal, for different parameter settings, and using different coupling strategies. To assess the MJO, a multivariate analysis based on OLR, precipitation, and the zonal wind components at 850 and 200 hPa in the tropical belt was performed. Multivariate EOF and frequency–wavenumber spectra were analyzed. Qualitatively and quantitatively ECHAM6, ECHAM5, and ECHAM4 are able to well represent the MJO. Among our simulations using the default Nordeng–Tiedtke scheme of ECHAM6, the coupled high-resolution (T127L95) experiments have the most realistic representation of the MJO. For those, we found a realistic strength of the eastward propagation. This represents a noteworthy improvement to the state of the art, as Lin et al. (2006) found that the strength of eastward propagation is mostly underestimated by the GCMs.

The character of the MJO in ECHAM is strongly determined by the representation of convection. In the AMIP-TIEDTKE experiment (without the modifications of Nordeng), the convective circulation system is distorted; the other experiments, all performed with the Nordeng modifications, show a well-structured eastward propagation of the envelope, consistent with the observed MJO. Hence, we conclude that the Nordeng modifications of the Tiedtke convection scheme (which principally renders convection more sensitive to free tropospheric moisture) are necessary in order to simulate an MJO in the ECHAM framework. Our results reveal some variability of the MJO. This is true among the members of the experiment groups, but also between different periods of the coupled experiments (not shown). This implies that the internal MJO variability has roughly the same magnitude as the variability in response to parameter changes. This is also shown in Mauritsen et al. (2012), where ensembles of ECHAM6 AMIP simulations also show variability of the MJO.

As in most other conventionally parameterized GCMs (Waliser et al. 2003, 2009; Zhang et al. 2006; Kim et al. 2009), the convection signal in the MJO of ECHAM6 is still too weak. At best the coupled simulations have about one-third of the variance of the reanalysis. In the AMIP experiments it is even lower (about one-quarter of the percentage relative to the reanalysis).

Besides the dominant impact of the representation of convection in ECHAM, our analysis reveals that factors such as coupling and resolution are also important for the character of the MJO. More specifically, we found the following: 1) The convective signal in the simulated MJO is enhanced by air–sea interaction. Thus, coupling improves the MJO. 2) The largest impact of resolution is on eastward propagation strength, which is enhanced by increasing resolution from T63L47 to T127L95. These findings are generally confirmed by ECHAM5.

Our results are obtained with a multivariate quantitative assessment approach, which we found is necessary for a sound assessment of simulated MJO. Based on the findings of our multivariable MJO analysis, we established a new MJO diagram and MJO metric that allow a quantitative comparison of simulated MJO. The metric and the diagram have been found helpful for model tuning and sensitivity studies with ECHAM6 experiments and may also prove useful in summarizing the simulation of the MJO in other models.

Acknowledgments. NCEP reanalysis and AVHRR OLR were provided by the National Oceanic and Atmospheric Administration (NOAA)-Cooperative Institute for Research in Environmental Sciences (CIRES) Earth System Research Laboratory (ESRL)/Physical Sciences Division (PSD) Climate Diagnostics Branch, Boulder, Colorado (http://www.cdc.noaa.gov).
We thank the ECMWF for providing the ERA-40 and ERA-Interim data. A study of this type was made possible through the efforts of the MJO working group, and their development of an MJO diagnostic package. This research was made possible through the support of the Max Planck Society for the Advancement of Science and the German Climate Computing Centre (Deutsches Klimarechenzentrum; DKRZ), Hamburg. The research leading to these results has received funding from the European Union, Seventh Framework Program (FP7/2007-2013) under Grant Agreement 244067. Jürgen Bader is thanked for his comments on an earlier draft of this article. We thank the anonymous reviewers for their careful reading of the manuscript and constructive comments.

REFERENCES

Benedict, J. J., and D. A. Randall, 2009: Structure of the Madden–Julian oscillation in the superparameterized CAM. *J. Atmos. Sci.,* **66,** 3277–3296.

——, and ——, 2011: Impacts of idealized air–sea coupling on Madden–Julian oscillation structure in the superparameterized CAM. *J. Atmos. Sci.,* **68,** 1990–2008.

Cassou, C., 2008: Intraseasonal interaction between the Madden–Julian oscillation and the North Atlantic Oscillation. *Nature,* **455,** 523–527.

Dee, D. P., and Coauthors, 2011: The ERA-Interim reanalysis: Configuration and performance of the data assimilation system. *Quart. J. Roy. Meteor. Soc.,* **137,** 553–597, doi:10.1002/qj.828.

Duchon, C. E., 1979: Lanczos filtering in one and two dimensions. *J. Appl. Meteor.,* **18,** 1016–1022.

Ferranti, L., T. N. Palmer, F. Molteni, and E. Klinker, 1990: Tropical–extratropical interaction associated with the 30–60 day oscillation and its impact on medium and extended range prediction. *J. Atmos. Sci.,* **47,** 2177–2199.

Goswami, B. N., R. S. Ajayamohan, P. K. Xavier, and D. Sengupta, 2003: Clustering of low pressure systems during the Indian summer monsoon by intraseasonal oscillations. *Geophys. Res. Lett.,* **30,** 1431, doi:10.1029/2002GL016734.

Hendon, H. H., 2000: Impact of air–sea coupling on the Madden–Julian oscillation in a general circulation model. *J. Atmos. Sci.,* **57,** 3939–3952.

Higgins, R. W., and K. Mo, 1997: Persistent North Pacific circulation anomalies and the tropical intraseasonal oscillation. *J. Climate,* **10,** 223–244.

Inness, P. M., J. M. Slingo, S. J. Woolnough, R. B. Neale, and V. D. Pope, 2001: Organization of tropical convection in a GCM with varying vertical resolution: Implications for the simulation of the Madden–Julian oscillation. *Climate Dyn.,* **17,** 777–793.

Jia, X., C. Li, J. Ling, and C. Zhang, 2008: Impacts of a GCM's resolution on MJO simulation. *Adv. Atmos. Sci.,* **25,** 139–156.

——, ——, N. Zhou and J. Ling, 2010: The MJO in an AGCM with three different cumulus parameterization schemes. *Dyn. Atmos. Oceans,* **49,** 141–163, doi:10.1016/j.dynatmoce.2009.02.003.

Jones, C., and L. Carvalho, 2002: Active and break phases in the South American monsoon system. *J. Climate,* **15,** 905–914.

Jungclaus J. H., and Coauthors, 2013: Characteristics of the ocean simulations in MPIOM, the ocean component of the MPI-Earth System Model. *J. Adv. Model. Earth Syst.,* doi:10.1002/jame.20023, in press.

Kalnay, E., and Coauthors, 1996: The NCEP/NCAR 40-Year Reanalysis Project. *Bull. Amer. Meteor. Soc.,* **77,** 437–471.

Khairoutdinov, M. F., and D. A. Randall, 2001: A cloud-resolving model as a cloud parameterization in the NCAR Community Climate System Model: Preliminary results. *Geophys. Res. Lett.,* **28,** 3617–3620.

Kim, D., and Coauthors, 2009: Application of MJO simulation diagnostics to climate models. *J. Climate,* **22,** 6413–6436.

——, A. Sobel, E. D. Maloney, D. M. W. Frierson, and I.-S. Kang, 2011: A systematic relationship between intraseasonal variability and mean state bias in AGCM simulations. *J. Climate,* **24,** 5506–5520.

Lau, W. K. M., 2005: ENSO connections. *Intraseasonal Variability of the Atmosphere–Ocean Climate System,* W. K. M. Lau and D. E. Waliser, Eds., Springer, 277–308.

Lee, M., I. Kang, and B. Mapes, 2003: Impacts of cumulus convection parameterization on aqua-planet AGCM Simulations of tropical intraseasonal variability. *J. Meteor. Soc. Japan,* **81,** 963–992, doi:10.2151/jmsj.81.963.

Liebmann, B., and C. Smith, 1996: Description of a complete (interpolated) OLR dataset. *Bull. Amer. Meteor. Soc.,* **77,** 1275–1277.

Liess, S., and L. Bengtsson, 2004: The intraseasonal oscillation in ECHAM4. Part II: Sensitivity studies. *Climate Dyn.,* **22,** 671–688.

——, ——, and K. Arpe, 2004: The intraseasonal oscillation in ECHAM4. Part I: Coupled to a comprehensive ocean model. *Climate Dyn.,* **22,** 653–669, doi:10.1007/s00382-004-0406-0.

Lin, J.-L., and Coauthors, 2006: Tropical intraseasonal variability in 14 IPCC AR4 climate models. Part I: Convective signals. *J. Climate,* **19,** 2665–2690.

Madden, R., and P. Julian, 1971: Detection of a 40–50-day oscillation in the zonal wind in the tropical Pacific. *J. Atmos. Sci.,* **28,** 702–708.

——, and ——, 1972: Description of global-scale circulation cells in the tropics with a 40–50-day period. *J. Atmos. Sci.,* **29,** 1109–1123.

——, and ——, 1994: Observations of the 40–50-day tropical oscillation: A review. *Mon. Wea. Rev.,* **112,** 814–837.

Majda, A. J., S. N. Stechmann, and B. Khouider, 2007: Madden–Julian oscillation analog and intraseasonal variability in a multicloud model above the equator. *Proc. Natl. Acad. Sci. USA,* **104,** 9919–9924.

Maloney, E. D., and D. L. Hartmann, 2001: The sensitivity of intraseasonal variability in the NCAR CCM3 to changes in convective parameterization. *J. Climate,* **14,** 2015–2034.

Matthews, A. J., B. J. Hoskins, and M. Masutani, 2004: The global response to tropical heating in the Madden–Julian oscillation during the northern winter. *Quart. J. Roy. Meteor. Soc.,* **130,** 1991–2011, doi:10.1256/qj.02.123.

Mauritsen, T., and Coauthors, 2012: Tuning the climate of a global model. *J. Adv. Model. Earth Syst.,* **4,** M00A01, doi:10.1029/2012MS000154.

McPhaden, M. J., 1999: Genesis and evolution of the 1997–98 El Niño. *Science,* **283,** 950–954.

Möbis, B., and B. Stevens, 2012: Mechanisms controlling the ITCZ placement in idealized simulations with ECHAM6. *J. Adv. Model. Earth Syst.,* **4,** M00A04, doi:10.1029/2012MS000199.

Newman, M., P. D. Sardeshmukh, and C. Penland, 2009: How important is air–sea coupling in ENSO and MJO evolution? *J. Climate,* **22,** 2958–2977.

Nordeng, T. E., 1994: Extended versions of the convective parameterization scheme at ECMWF and their impact on the mean and transient activity of the model in the tropics. ECMWF Tech. Memo. 206, 41 pp.

Park, C.-K., D. M. Straus, and K.-M. Lau, 1990: An evaluation of the structure of tropical intraseasonal oscillations in three general circulation models. *J. Meteor. Soc. Japan,* **68,** 403–417.

Pohl, B., and A. J. Matthews, 2007: Observed changes in the lifetime and amplitude of the Madden–Julian oscillation associated with interannual ENSO sea surface temperature anomalies. *J. Climate,* **20,** 2659–2674.

Randall, D., M. Khairoutdinov, A. Arakawa, and W. Grabowski, 2003: Breaking the cloud parameterization deadlock. *Bull. Amer. Meteor. Soc.,* **84,** 1547–1564.

Roeckner, E., and Coauthors, 2003: The atmospheric general circulation model ECHAM 5. Part I: Model description. MPI Rep. 349, 140 pp. [Available online at http://www.mpimet.mpg.de/fileadmin/publikationen/Reports/max_scirep_349.pdf.]

Sato, N., C. Takahashi, A. Seiki, K. Yoneyama, R. Shirooka, and Y. N. Takayabu, 2009: An evaluation of the reproducibility of the Madden–Julian oscillation in the CMIP3 multi-models. *J. Meteor. Soc. Japan,* **87,** 791–805.

Slingo, J. M., and Coauthors, 1996: Intraseasonal oscillations in 15 atmospheric general circulation models: Results from an AMIP diagnostic subproject. *Climate Dyn.,* **12,** 325–357.

——, P. Inness, and K. Sperber, 2005: Modeling. *Intraseasonal Variability of the Atmosphere–Ocean Climate System,* W. K. M. Lau and D. E. Waliser, Eds., Springer, 361–388.

Sobel, A. H., E. D. Maloney, G. Bellon, and D. M. Frierson, 2010: Surface fluxes and tropical intraseasonal variability: A reassessment. *J. Adv. Model. Earth Syst,* **2** (2), doi:10.3894/JAMES.2010.2.2.

Sperber, K. R., 2004: The Madden–Julian oscillation. An appraisal of coupled climate model simulations, PCMDI Rep. UCRL-TR-202550, Lawrence Livermore National Laboratory, 146–158.

——, and H. Annamalai, 2008: Coupled model simulations of boreal summer intraseasonal (30–50 day) variability, Part 1: Systematic errors and caution on use of metrics. *Climate Dyn.,* **31,** 345–372, doi:10.1007/s00382-008-0367-9.

——, S. Gualdi, S. Legutke, and V. Gayler, 2005: The Madden–Julian oscillation in ECHAM4 coupled and uncoupled general circulation models. *Climate Dyn.,* **25,** 117–140.

Stevens, B., and Coauthors, 2013: ECHAM6—Model and climate. *J. Adv. Model. Earth Syst.,* in press.

Straub, K. H., G. N. Kiladis, and P. E. Ciesielski, 2006: The role of equatorial waves in the onset of the South China Sea summer monsoon and the demise of El Niño during 1998. *Dyn. Atmos. Oceans,* **42,** 216–238.

Subramanian, A. C., M. Jochum, A. J. Miller, R. Murtugudde, R. B. Neale, and D. E. Waliser, 2011: The Madden–Julian oscillation in CCSM4. *J. Climate,* **24,** 6261–6282.

Takayabu, Y. N., T. Iguchi, M. Kachi, A. Shibata, and H. Kanzawa, 1999: Abrupt termination of the 1997–98 El Niño in response to a Madden–Julian oscillation. *Nature,* **402,** 279–282.

Teng, H., and B. Wang, 2003: Interannual variations of the boreal summer intraseasonal oscillation in the Asian–Pacific region. *J. Climate,* **16,** 3572–3584.

Tiedtke, M., 1989: A comprehensive mass flux scheme for cumulus parameterization in large-scale models. *Mon. Wea. Rev.,* **117,** 1779–1800.

——, 1993: Representation of clouds in large-scale models. *Mon. Wea. Rev.,* **121,** 3040–3061.

Uppala, S. M., and Coauthors, 2005: The ERA-40 Re-Analysis. *Quart. J. Roy. Meteor. Soc.,* **131,** 2961–3012, doi:10.1256/qj.04.176.

Vitart, F., F. Molteni, and T. Jung, 2011: Prediction of the Madden–Julian oscillation and its impact on the European weather in the ECMWF monthly forecasts. *Proc. ECMWF Seminar on Predictability in the European and Atlantic Regions from Days to Years,* ECMWF. [Available online at http://www.ecmwf.int/newsevents/meetings/annual_seminar/2010/presentations/Vitart.pdf.]

von Storch, H., and F. W. Zwiers, 1999: *Statistical Analysis in Climate Research.* Cambridge University Press, 494 pp.

Waliser, D. E., K. M. Lau, and J. H. Kim, 1999: The influence of coupled sea surface temperatures on the Madden–Julian oscillation: A model perturbation experiment. *J. Atmos. Sci.,* **56,** 333–358.

——, and Coauthors, 2003: AGCM simulations of intraseasonal variability associated with the Asian summer monsoon. *Climate Dyn.,* **21,** 423–446.

——, and Coauthors, 2009: MJO simulation diagnostics. *J. Climate,* **22,** 3006–3030.

Wheeler, M. C., and H. H. Hendon, 2004: An all-season real-time multivariate MJO index: Development of an index for monitoring and prediction. *Mon. Wea. Rev.,* **132,** 1917–1932.

——, and J. L. McBride, 2005: Australian–Indonesian monsoon. *Intraseasonal Variability in the Atmosphere–Ocean Climate System,* W. K. M. Lau and D. E. Waliser, Eds., Springer, 125–173.

Woolnough, S. J., F. Vitard, and M. A. Balmaseda, 2007: The role of the ocean in the Madden–Julian oscillation: Implications for MJO prediction. *Quart. J. Roy. Meteor. Soc.,* **133,** 117–128.

Zhang, C., 2005: Madden–Julian oscillation. *Rev. Geophys.,* **43,** RG2003, doi:10.1029/2004RG000158.

——, and J. Gottschalck, 2002: SST anomalies of ENSO and the Madden–Julian oscillation in the equatorial Pacific. *J. Climate,* **15,** 2429–2445.

——, M. Dong, S. Gualdi, H. H. Hendon, E. D. Maloney, A. Marshall, K. R. Sperber, and W. Wang, 2006: Simulations of the Madden–Julian oscillation in four pairs of coupled and uncoupled global models. *Climate Dyn.,* **27,** 573–592.

Zhu, H., H. Hendon, and C. Jakob, 2009: Convection in a parameterized and superparameterized model and its role in the representation of the MJO. *J. Atmos. Sci.,* **66,** 2796–2811.